# Electromagnon in the Y-type hexaferrite $BaSrCoZnFe_{11}AlO_{22}$

Jakub Vít,[1,2,3,*] Filip Kadlec,[1] Christelle Kadlec,[1] Fedir Borodavka,[1] Yi Sheng Chai,[4,5] Kun Zhai,[4] Young Sun,[4] and Stanislav Kamba[1,*]

[1]*Institute of Physics of the Czech Academy of Sciences, Na Slovance 2, 182 21 Prague 8, Czech Republic*

[2]*Faculty of Nuclear Science and Physical Engineering, Czech Technical University, Břehová 7, 115 19 Prague 1, Czech Republic*

[3]*Department of Physics, Budapest University of Technology and Economics and MTA-BME Lendület Magneto-optical Spectroscopy Research Group, 1111 Budapest, Hungary*

[4]*Institute of Physics, Chinese Academy of Sciences, Beijing 100190, P. R. China*

[5]*Department of Applied Physics, Chongqing University, Chongqing 401331, P. R. China*

(Received 19 December 2017; revised manuscript received 14 February 2018; published 9 April 2018)

We investigated static and dynamic magnetoelectric properties of single crystalline $BaSrCoZnFe_{11}AlO_{22}$, which is a room-temperature multiferroic with Y-type hexaferrite crystal structure. Below 300 K, a purely electric-dipole-active electromagnon at ≈1.2 THz with the electric polarization oscillating along the hexagonal axis was observed by THz and Raman spectroscopies. We investigated the behavior of the electromagnon with applied dc magnetic field and linked its properties to static measurements of the magnetic structure. Our analytical calculations determined selection rules for electromagnons activated by the magnetostriction mechanism in various magnetic structures of Y-type hexaferrite. Comparison with our experiment supports that the electromagnon is indeed activated by the magnetostriction mechanism involving spin vibrations along the hexagonal axis.

DOI: 10.1103/PhysRevB.97.134406

## I. INTRODUCTION

Magnetoelectric (ME) multiferroics are fascinating materials due to a potential possibility of achieving an electric control of their magnetic states. The group of hexaferrites, i.e., iron oxides with hexagonal crystal structures, look promising in view of their high operating temperatures and huge ME effects [1–4] owing to their magnetic structures being very sensitive to the chemical composition and low external magnetic field [2,5,6].

In terms of crystal structures, hexaferrites are classified as M, Y, Z type, etc., depending on the stacking sequence of basic *crystallographic* blocks along the hexagonal axis [2,7]. Owing to their complexity, the magnetic structures determined by neutron diffraction are usually described via different, *magnetic* blocks also aligned along the hexagonal axis, denoted as L and S, possessing large and small magnetic moments, respectively [5,8–10]. Within each individual block, the magnetic moments are collinearly aligned [2]. Hexaferrites mostly possess ferrimagnetic structures; in some cases, the moments may compensate and yield a zero net magnetic moment [11], but mostly, the magnetic structures may easily become ferrimagnetic upon applying moderate magnetic fields. The magnetic frustration due to the competing superexchange interaction across the boundary between L and S blocks often yields a noncollinear alignment of spins, leading to the transverse conical (TC) spin structure [Fig. 1(g)] which induces the electric dipole moment. This phenomenon can be explained by the inverse Dzyaloshinskii-Moriya (iDM) interaction [12] or Katsura-Nagaosa-Balatsky model [13]: $\vec{P} = \sum_{i,j} P_{i,j} \cdot \vec{e}_{i,j} \times (\vec{S}_i \times \vec{S}_j)$. In contrast, the electric dipole moments induced by the iDM interaction cancel out in the longitudinal conical (LC) spin structures [Figs. 1(d) and 1(e)] where no net polarization is observed.

The first discovered ME hexaferrite was the Y-type $Ba_{0.5}Sr_{1.5}Zn_2Fe_{11}O_{22}$ reported by Kimura *et al.* [14]. Later, Wang *et al.* [6] studied a compound with a similar composition, $BaSrCoZnFe_{11}AlO_{22}$, which we study in this paper, showing a stronger ME effect at higher temperatures. Near 400 K, its paramagnetic structure transforms to a collinear ferrimagnetic one with spins aligned within the *ab* plane [15]. Below $T_{con} \approx 365$ K, the proper-screw [also called transverse spiral, Fig. 1(c)] magnetic structure is established [6]. On zero-field cooling (ZFC), the spins start to tilt from the hexagonal plane, giving rise to one of the LC structures.

In a part of the $Ba_xSr_{2-x}Zn_yCo_{2-y}Fe_{11+z}Al_{1-z}O_{22}$ compounds, two types of LC structures were identified [10,11,16]: (i) The normal longitudinal conical [NLC, Fig. 1(e)], which is stable when the values of $\mu_0 \boldsymbol{H} \parallel c$ lie within cca. 2–5 T, and (ii) the alternating longitudinal conical [ALC, Fig. 1(d)], which is observed at lower fields ($\mu_0 \boldsymbol{H} \lesssim 2$ T), where the *c* components of the magnetic moments are aligned as ↑-0-↓-0 [10] or ↑-↑-↓-↓ [16], leading to a zero net magnetic moment. The latter spin configuration gives rise to ferroelectricity even at room temperature due to the magnetostriction (also called exchange-striction) mechanism $\vec{P} = \sum_{i,j} \vec{P}_{i,j}(\vec{S}_i \cdot \vec{S}_j)$ [16]. In both NLC and ALC structures, the spin modulations point along the *c* axis with a commensurate ordering of cones—$\boldsymbol{Q}_C = (0,0,1.5)$ for the ALC structure and $\boldsymbol{Q}_C = (0,0,3)$ for the NLC structure—and an incommensurate one $\boldsymbol{Q}_{IC} = (0,0,q)$ describing the helical angle dependence. The first-order metamagnetic transition between the NLC and ALC structures shows a remarkable hysteresis [10,16]. With increasing $\boldsymbol{H} \parallel c$,

*Authors to whom correspondence should be addressed: vit@fzu.cz, kamba@fzu.cz

 

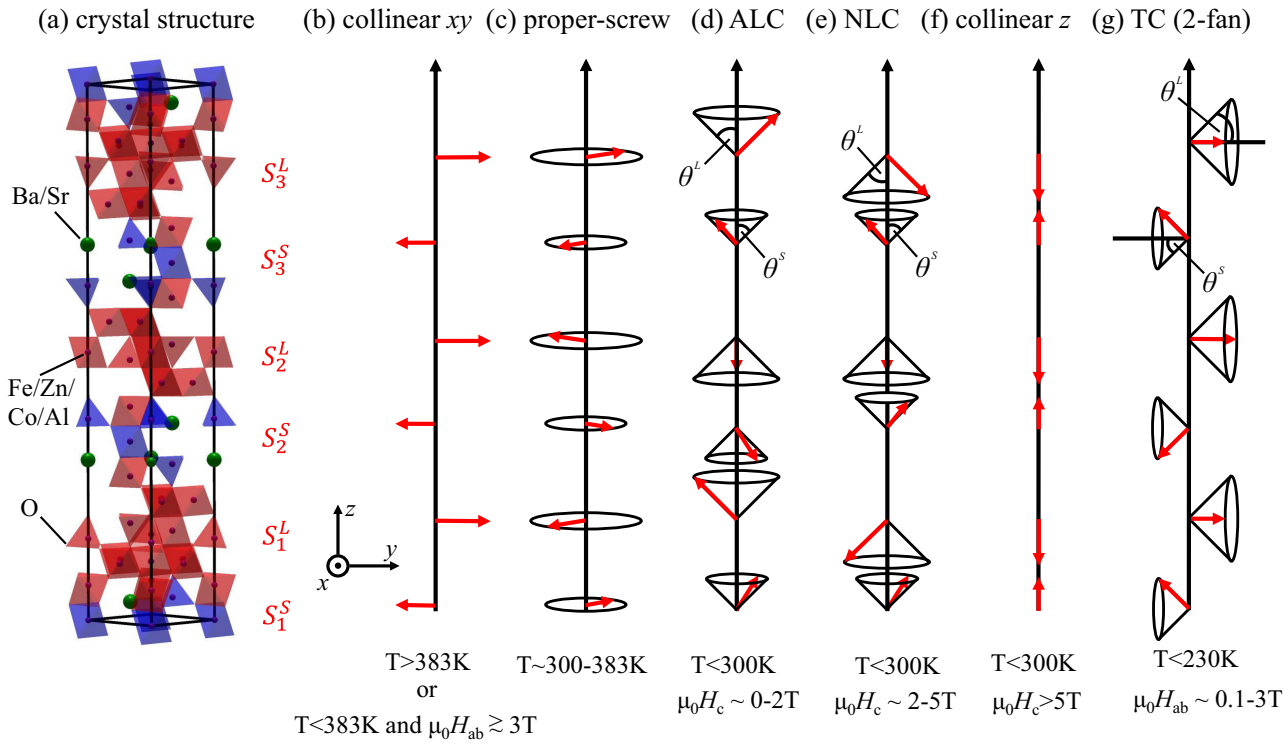


FIG. 1. (a) Crystal and [(b)–(g)] magnetic structures of the Y hexaferrite $BaSrCoZnFe_{11}AlO_{22}$. Below each magnetic structure, its occurrence in the $(H,T)$ phase diagram is marked.

the conical angle of the NLC structure decreases and it vanishes at $\mu_0 \boldsymbol{H} \approx 5$ T in $BaSrCoZnFe_{11}AlO_{22}$. Around this value, the magnetization saturates and the magnetic structure transforms to the collinear ferrimagnetic, as the magnetic moments of the L and S blocks, pointing along the $c$ axis, become antiparallel [6]. In this case no ferroelectric polarization is induced.

When applying the magnetic field in the magnetically isotropic $ab$ plane, the TC structure with a modulation vector $\boldsymbol{Q}_C = (0,0,1.5)$ is established [10,11,16], giving rise to electric polarization due to the iDM interaction [17]. According to the iDM term, the polarization is perpendicular to both the $c$ axis and the magnetic field. The sign of the polarization is given by the helicity of the spin structure, which is determined by the cross product of electric and magnetic poling fields [3]. When rotating the magnetic field within the $ab$ plane, the polarization rotates the same way [14]. When the magnetic field is reversed in the $ab$ plane, two cases may occur [18]: (i) If the TC phase remains metastable at zero field (case of lower temperatures), then the cones' axes rotate in the $ab$ plane conserving the helicity and, subsequently, the polarization is reversed. (ii) If the TC structure is unstable in the low-field region even after $ab$-field poling (at higher temperatures), then the cone axes rotate through the $c$ axis (yielding the ALC structure which is stable after ZFC). Consequently, the helicity is reversed, and the polarization is recovered with the same sign after a magnetic field switch [18].

The dynamic ME effect exhibits resonances called electromagnons. These are electric-dipole-active excitations represented by collective spin motions, believed to be caused by the same types of microscopic mechanisms as the static ME effect, linked to the ground-state magnetic structure. However, electromagnons involve both ground and excited states, thus obeying different selection rules than the static ME effect [19]. It is important to note that electromagnons do not have to be magnetic-dipole active; i.e., they may represent changes in the magnetic quadrupole (or higher-order multipole) moments where no net magnetization is changed. An analogy is known from lattice dynamics, where some phonons can be nonpolar.

The first electromagnon in hexaferrites, reported in $Ba_2Mg_2Fe_{12}O_{22}$ in the THz range, was attributed to the magnetostriction mechanism [20]. In $BaSrCo_2Fe_{11}AlO_{22}$, a compound very similar to $BaSrCoZnFe_{11}AlO_{22}$ investigated here, a similar spin excitation was also observed by inelastic neutron scattering [10] but not yet by THz spectroscopy, which would confirm its electric-dipole activity. Nakajima *et al.* [10] only suggested that the spin excitation could be an electromagnon, since the magnetic structure allows its activation in the THz dielectric spectra via the magnetostriction mechanism. The leading terms contributing to the dynamical electric polarization $\vec{P}$ are of the type $\vec{P} \propto \vec{S}_i \cdot \delta\vec{S}_j$, where $\delta\vec{S}_j$ represents fluctuations of the neighboring spin j. Since $\delta\vec{S}_j$ is perpendicular to $\vec{S}_j$, the term is higher when the spins are less collinear, in contrast to the static magnetostriction, proportional to $\vec{S}_i \cdot \vec{S}_j$, whose effect is the highest in collinear structures. Nakajima *et al.* [10,21] proposed that the spin excitations in $Ba_2Mg_2Fe_{12}O_{22}$ and $BaSrCo_2Fe_{11}AlO_{22}$ correspond to spins oscillations without an influence on the overall magnetic dipole moment; only the quadrupole moment can be changed. Then, the possible electromagnon in $BaSrCo_2Fe_{11}AlO_{22}$ would be purely electric-dipole active in the THz (or infrared) spectra. Such a coupling between the

magnetic quadrupole and the electric dipole moments with the same symmetry can be explained by theory based on symmetry [19,22].

Here we study ME properties of $BaSrCoZnFe_{11}AlO_{22}$ single crystals. We combined different static and dynamic measurements in magnetic field applied both within and perpendicular to the hexagonal plane to explore the $(T,H)$ phase diagram, including the TC, ALC, NLC, proper-screw, and collinear ferrimagnetic phases. The static measurements include magnetization curves and magnetic-field-dependent permittivity; the dynamic properties were probed by THz, infrared, and Raman spectroscopies providing access to excitations with different selection rules. In all measurements, the magnetic field history was recorded, as it may have an influence on the physical properties of the samples. We observed an electromagnon and thoroughly studied its behavior depending on the magnetic field direction and history. The electromagnon strength is clearly correlated with the static magnetic measurements reflecting the magnetic structure, which gives us a tool to check the selection rules activating the electromagnon, including quantitative evaluation. By comparing the analytically calculated electric polarization with the measured electromagnon strength in all observed magnetic phases, we conclude that the electromagnon is most probably caused by the magnetostriction mechanism, as proposed earlier, whereas the spins vibrate along the hexagonal axis.

## II. SAMPLES AND EXPERIMENTAL DETAILS

$BaSrCoZnFe_{11}AlO_{22}$ single crystals were grown by the flux method [23]. The samples were measured as grown except for magnetic-field-dependent permittivity, before which the samples were annealed in an oxygen atmosphere at 900 °C for 7 days. The exact composition was determined by energy-dispersive analysis of x rays as $Ba_{1.1}Sr_{0.9}Co_{1.3}Zn_{0.7}Fe_{11}AlO_{22}$.

THz complex transmittance from 0.2 to 2.3 THz was measured using a custom-made time-domain spectrometer powered by a Ti:sapphire femtosecond laser with 35-fs-long pulses centered at 800 nm. The system is based on coherent generation and subsequent coherent detection of ultrashort THz transients [24]. The detection scheme is realized on an electro-optic sampling of the electric field of the transients within a 1-mm-thick, (110)-oriented ZnTe crystal as a sensor. This allows us to measure time profile of the THz transients transmitted through a studied sample. Details about the calculations of complex index of refraction can be found in Ref. [24]. Spectra were obtained with resolution better than 0.1 THz. For the low-temperature THz complex transmittance and IR reflectivity spectroscopies, an Oxford Instruments Optistat optical continuous He-flow cryostats with mylar and polyethylene windows, respectively, were used. THz spectroscopy with magnetic field was performed using another custom-made time-domain spectrometer comprising an Oxford Instruments Spectromag cryostat with a superconducting magnet, allowing us to apply an external magnetic field of up to 7 T in both Voigt and Faraday geometries.

For Raman studies, a Renishaw RM 1000 Micro-Raman spectrometer equipped with a charged-coupled device (CCD) detector and Bragg filters was used. The experiments were performed using an $Ar^+$ ion laser (wavelength of 514.5 nm) in the backscattering geometry within the 0.3- to 24-THz range, in an Oxford Instruments Microstat continuous-flow optical He cryostat. Further, using a Quantum design MPMS and PPMS instruments equipped with the Andeen-Hagerling 2500A high-precision capacitance bridge, we carried out measurements of magnetization and of magnetic-field-dependent permittivity in a temperature interval from 5 to 400 K, with a magnetic field of up to 7 T.

Low-temperature IR reflectivity measurements in the frequency range 1–20 THz were performed using a Bruker IFS-113v Fourier-transform IR spectrometer equipped with a liquid-He-cooled Si bolometer (1.6 K) serving as a detector. Room-temperature mid-IR spectra up to 150 THz were obtained using a pyroelectric deuterated triglycine sulfate detector.

## III. RESULTS AND DISCUSSION

### A. Magnetization measurements

Since several neutron diffraction studies of $Ba_xSr_{2-x}Co_yZn_{2-y}Fe_{11+z}Al_{1-z}O_{22}$ Y-type hexaferrites determined their magnetic structures and correlated them with magnetization data [10,11,16], it is possible to determine the magnetic structures of our sample just from measurements of magnetic-field-dependent magnetization and permittivity.

To verify the presence of conical structures, we measured the temperature-dependent magnetization for $\boldsymbol{H} \parallel c$ and $\boldsymbol{H} \perp c$ [25]. The phase transition from the collinear to the proper-screw structure was revealed at 383 K (Fig. S1 in Ref. [25]) which is in agreement with previous results, as the temperature of the phase transition is sensitive to chemical composition [15]. After $\boldsymbol{H} \perp c$ poling at $T \approx 10$ K, the TC structure remains stable up to 230 K even at $\boldsymbol{H} = 0$ (see Ref. [25] and Fig. S1 therein), which is consistent with the previous work of Shen *et al.* [26].

Two magnetic structures, the NLC and ALC, were reported to exist after ZFC in $Ba_xSr_{2-x}Co_yZn_{2-y}Fe_{11+z}Al_{1-z}O_{22}$ [16,21]. To identify the one present in our samples at low temperatures, we measured magnetization along the $c$ axis at 10 K [Fig. 2(a)]. We observed a curve with a remarkable hysteresis up to ≈4 T similar to that observed by Shen *et al.* [26], indicating that the ALC structure is the ground state after ZFC. If the NLC structure were the ground state, then the hysteresis would not extend to such a high magnetic field, since the NLC structure continuously transforms into the high-field collinear phase. A hysteresis coming from domain switching would be expected only at low fields, as it is the case of magnetization in the $ab$ plane (Fig. 3). From the comparison of our magnetization curve and of the magnetic-field-dependent permittivity [Figs. 2(a) and 2(b)] with the work of Shen *et al.* [16], we can claim that the ALC structure persists up to ≈4 T if coming from low-field region, and it recovers only when the field is decreased to ≈1 T. A similar behavior was observed at temperatures up to 200 K, so we expect the ALC structure to exist in this temperature region at zero field after ZFC. The existence of the ALC structure after ZFC is also supported by THz and Raman measurements (see text below). At higher fields, the NLC structure appears, and it continuously transforms into, the collinear ferrimagnetic structure with spins along the $c$ axis.

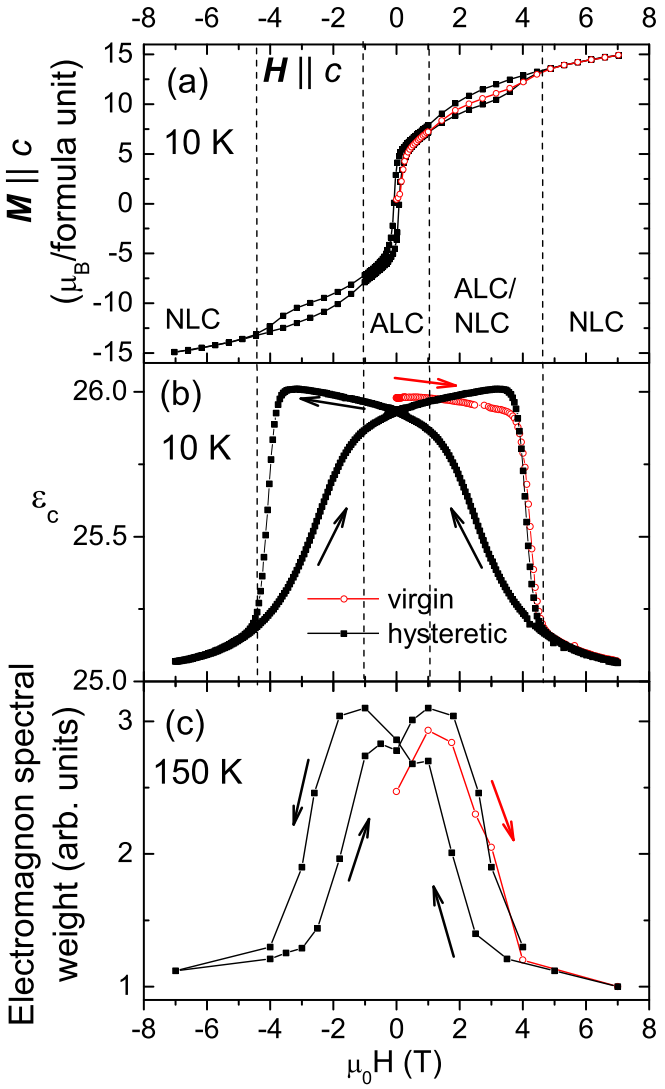


FIG. 2. (a) Magnetization per formula unit, (b) permittivity at 1 kHz and (c) spectral weight of the electromagnon as a function of $\boldsymbol{H} \parallel c$ calculated from THz $k(\omega)$ spectra. Red curves correspond to virgin magnetization curves after ZFC. Note that at $T = 10$ K and $T = 150$ K the phase diagram is qualitatively the same and therefore, we can compare both measurements.

After applying $\boldsymbol{H}$ in the $ab$ plane, the TC structure is known to establish in $BaSrCoZnFe_{11}AlO_{22}$ [3]. In such a case, we observe the virgin magnetization curve outside the hysteresis loop (Fig. 3); this means that after ZFC, the sample has an easy $c$-axis anisotropy, which is consistent with the ALC structure. After a high-field treatment, the zero-field susceptibility is high and it shows only a tiny hysteresis, indicating an easy-plane anisotropy. At 0.3 T, the virgin curve coincides with the hysteretic one, which is then the field sufficient to establish the TC structure. This result is consistent with the TC structure persisting also in zero field after applying high $\boldsymbol{H} \perp c$, as reported before in Ref. [26].

### B. Electromagnon in zero field cooling

We measured polarized THz transmittance of $BaSrCoZnFe_{11}AlO_{22}$ (001)- and (100)-oriented crystal plates,

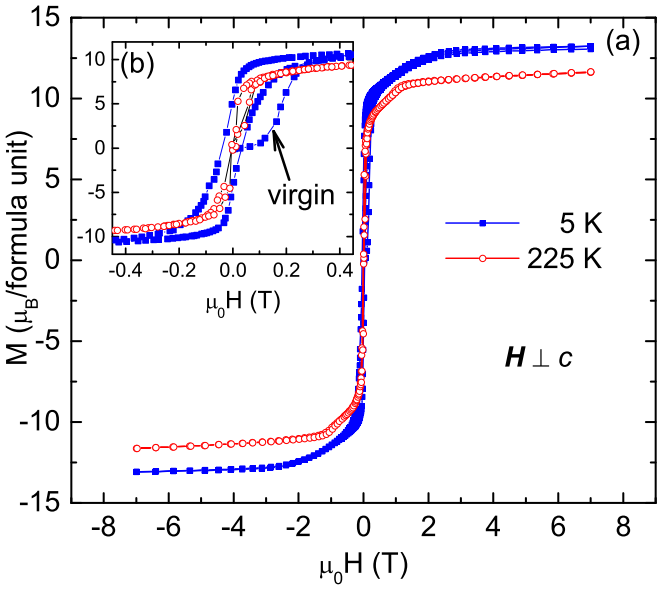


FIG. 3. (a) Magnetization curve for $\boldsymbol{H} \parallel [100]$. The inset (b) shows the detailed $M(H)$ dependence at low fields revealing the magnetization after leaving the virgin state reached by ZFC.

providing a complete set of spectra at temperatures from room temperature down to 8 K. At ≈1.2 THz, we observed an excitation present exclusively in the $\boldsymbol{E}^{\omega} \parallel c$ polarization (Fig. 4), implying it is purely electric-dipole active. If it were magnetically active, then it would be present also in the $\boldsymbol{E}^{\omega} \perp c$, $\boldsymbol{H}^{\omega} \perp c$ polarized spectra; however, THz spectra in other polarizations show no remarkable features (see Figs. S2 and S3 in the Supplemental Material [25]). This polar excitation is relatively weak and overdamped at room temperature, whereas on cooling, its damping decreases and its frequency and intensity rise. As we show below, this excitation strongly depends on magnetic field, and therefore, it has a magnetic origin. Consequently, this is an electromagnon, similar to that observed in $Ba_2Mg_2Fe_{12}O_{22}$ [20,21,27] and to a possible one in $BaSrCo_2Fe_{11}AlO_{22}$ [10]. In contrast to $Ba_2Mg_2Fe_{12}O_{22}$, where the electromagnon was revealed below ≈100 K [27,28], we observed the corresponding absorption up to 300 K. On heating, the ALC structure gradually transforms to the proper-screw one, where the electromagnon is inactive due to the symmetry (see Table I); therefore its strength gradually decreases. At 383 K, the magnetic structure changes from the proper-screw one to the collinear one, where the electromagnon is also forbidden by symmetry (see Table I).

Investigating the THz spectra in more detail, we see a clear double-peak structure in the imaginary part of the refractive index $k(\omega)$ [Fig. 4(b)] at 200 K. At higher temperatures, the peaks are also asymmetric. Below 200 K, the transmission signal around the peak in $k(\omega)$ is low which prevents us from reliably determining the peak shape [29]. The double-peak structure at higher temperatures does not imply the same feature at lower temperatures—it may imply a mixture of magnetic phases, while at low temperatures, usually a single phase is established. The mixed phase was recently reported by Shen *et al.* [16], but only after a magnetic field treatment.

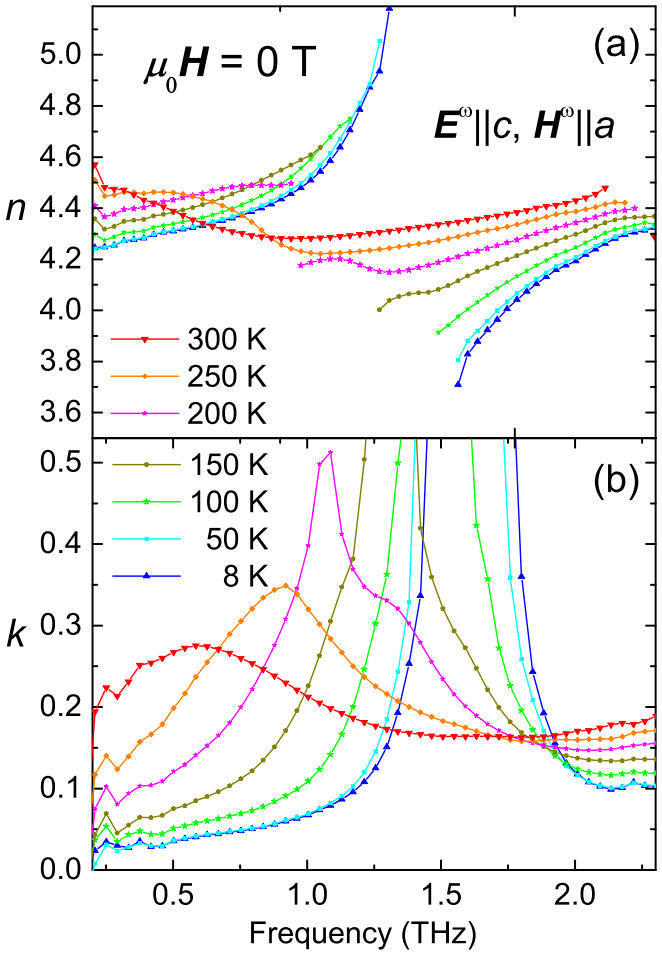


FIG. 4. Temperature-dependent THz spectra of (a) real and (b) imaginary part of the refractive index in $\boldsymbol{E}^\omega \parallel c$, $\boldsymbol{H}^\omega \parallel a$ polarization. Below 200 K, the parts of the spectra exhibiting high absorption due to the electromagnon are missing.

We therefore believe that the double-peak structure persists to low temperatures, and we then see two electromagnon modes with similar frequencies in the pure ALC phase.

To get more complete knowledge about activity of the electromagnon in various spectra, we measured temperature-dependent polarized Raman spectra (Fig. 5 and Figs. S7, S8, and S9 in the Supplemental Material [25]). In the $a(cc)\bar{a}$-polarized spectra, we clearly see the same electromagnon as in THz spectra. Note also its asymmetric shape confirming its doublet character. Assuming the parent paraelectric space group $D_{3d}^5 - R\bar{3}m$ [6], the factor-group analysis of Brillouin-zone-center phonons reads [30]

$$\begin{aligned}\Gamma_{D_{3d}^5} &= 14A_{1g}(a^2+b^2,c^2)\\ &+ 4A_{1u}(-) + 4A_{2g}(-) + 16A_{2u}(c)\\ &+ 18E_g(a^2-b^2,ab,ac,bc) + 20E_u(a,b). \quad (1)\end{aligned}$$

In such case, the polar $\boldsymbol{E}^\omega \parallel c$-active electromagnon should follow the same selection rules as the $A_{2u}$ symmetry polar phonon—it would be present in the THz spectra but absent in any Raman spectra. Since we see the electromagnon also in $c^2$-polarized Raman spectra, the magnetic and crystal structures must be noncentrosymmetric below ≈300 K where the electromagnon is observed. It is known that the NLC magnetic phase is centrosymmetric, but the ALC magnetic structure with the ↑-↑-↓-↓ spin configuration along the $c$ axis breaks the inversion symmetry and, in the case of ME coupling, induces electric polarization $\boldsymbol{P} \parallel c$ in a low-field region, including $\boldsymbol{H} = 0$ where this structure exists [16]. Therefore, its point group must be polar $C_{3v}$ and the factor group analysis of phonons reads

$$\begin{aligned}\Gamma_{C_{3v}} &= 30A_1(c,a^2+b^2,c^2) + 8A_2(-)\\ &+ 38E(a,b,a^2-b^2,ab,ac,bc). \quad (2)\end{aligned}$$

In this phase, polar phonons and electromagnons have the same $A_1$ symmetry and they are active in both $\boldsymbol{E}^\omega \parallel c$-polarized IR or THz spectra and $c^2$, $a^2$, and $b^2$ Raman spectra, as confirmed by our experiment (see Fig. 5 and Ref. [25]). The statement that in acentric ferroelectric phases electromagnons should be both IR and Raman active was expressed and confirmed first by Skiadopoulou *et al.* for the case of $BiFeO_3$ [31]. Nevertheless, in Raman spectra of $BiFeO_3$ electromagnons are much weaker than phonons [32], while in Y-type hexaferrite the electromagnon is stronger than any phonon (Fig. S7 in Ref. [25]). It can be explained by the different mechanism of their activation: Electromagnons in $BiFeO_3$ are induced by iDM interaction, which originates in the spin-orbital coupling which is a weak effect [33,34]; and the dynamical polarization comes from the electronic polarization [13] which cannot reach as high values as the ionic one. In contrast, the electromagnon in our sample is activated by magnetostriction (see subsection E below) and this spin-lattice coupling gives the ionic polarization which can be stronger. However, more importantly, this ionic, magnetostriction-induced polarization can be a subject of high fluctuations, crucial for high Raman intensity: This comes from the extremely high susceptibility of the frustrated magnetic structures, allowing spin fluctuations with high amplitudes, which is very distinct from the case of $BiFeO_3$. Also the pure magnetic origin is unlikely to be the reason for the presence of an electromagnon in Raman spectra [35]. A more detailed discussion of the high Raman intensity of the electromagnon can be found in the Supplemental Material [25], and the IR and Raman phonon spectra will be presented elsewhere [36].

### C. Evolution of the electromagnon on $H \perp c$

Below 270 K, we measured polarized THz spectra in external dc magnetic field, which stabilizes the TC structure below ≈230 K. The magnetic-field dependence is qualitatively the same within the whole temperature range; below we discuss the spectra at 150 K where the transmission at the peak position is still above the noise level (Fig. 6). The strength of the electromagnon gradually decreases with $\boldsymbol{H} \perp c$, becoming small above 2 T and negligible above 4 T. This corresponds to the continuous phase transition into the collinear ferrimagnetic structure and it is consistent with the assumption that the electromagnon is induced by magnetostriction in the ALC and TC magnetic structures. In the high-field collinear phase, the fluctuations $\delta\vec{S}_i$ are perpendicular to all $\vec{S}_j$, and their scalar

TABLE I. Analytically calculated activity of electromagnons in $\boldsymbol{E}^{\omega} \parallel c$ spectra induced by the magnetostriction in the Y-type hexaferrite with various magnetic structures. $S^L$ and $S^S$ are the magnitudes of large and small spins, respectively; $\theta^L$ and $\theta^S$ are the conical angles taken from the conical axes ($z$ in the case of the NLC and ALC structures and $y$ in the TC structure); $(\delta S_1^j)_i$ denote spin deviations along $i = x, y, z$ for small and large spin blocks, marked as $j = S$ and $L$, respectively. The proper-screw structure can be taken as a degenerate ALC (or NLC) structure for $\theta^L = \theta^S = 0$, giving no electromagnon mode.

| Magnetic structure | Oscillating polarization according to Eq. (3): $P_z(t) \propto$ | Distinct modes | Constraints |
|---|---|---|---|
| 2-fan (TC) | $4S^L \sin(\theta^L)(\delta S_1^S)_x$ | $x$ mode | $(\delta S_1^S)_x \propto S^S$ |
| | $+0(\delta S_1^S)_y$ | – | |
| | $+4S^S \sin(\theta^S)(\delta S_1^L)_z$ | $z$ mode | $(\delta S_1^L)_z \propto S^L$ |
| ALC | $2\sqrt{2}[S^L \sin(\theta^L)(\delta S_1^S)_x + S^S \sin(\theta^S)(\delta S_1^L)_x]$ | $xy$ mode | |
| | $+2\sqrt{2}[S^L \sin(\theta^L)(\delta S_1^S)_y + S^S \sin(\theta^S)(\delta S_1^L)_y]$ | | |
| | $+4S^L \cos(\theta^L)(\delta S_1^S)_z + 4S^S \cos(\theta^S)(\delta S_1^L)_z$ | $z$ mode | $(\delta S_1^S)_z \propto S^S \sin(\theta^S)$, $(\delta S_1^L)_z \propto S^L \cdot \sin(\theta^L)$ |
| NLC | $2\sqrt{2}[S^L \sin(\theta^L)(\delta S_1^S)_x + S^S \sin(\theta^S)(\delta S_1^L)_x]$ | $xy$ mode | |
| | $+2\sqrt{2}[S^L \sin(\theta^L)(\delta S_1^S)_y + S^S \sin(\theta^S)(\delta S_1^L)_y]$ | | |
| | $+0(\delta S_1^S)_z + 0(\delta S_1^L)_z$ | – | |
| Collinear | 0 | – | |

products are then practically zero; thus the electromagnon vanishes. Also the gradual decrease in its strength is consistent with the expectations—in the TC structure, for a mode corresponding to spin vibrations along the $c$ axis, its strength should be proportional to the sine of the conical angle $\theta^S$ (between the spins and the conical axis in the hexagonal plane; see Table I and Fig. 1), and the angle $\theta^S$ decreases to zero with increasing magnetic field.

Further, we see a low-frequency resonance which appears at 4 T at ≈0.2 THz and whose frequency increases linearly with the magnetic field with a slope of ca. 0.05 THz/T. Although this resonance reminds of a ferrimagnetic resonance observed in Z-type hexaferrite [37], a detailed analysis reveals a different behavior: First, the slope is much higher than the gyromagnetic ratio for a free electron, $\gamma_0 = 0.028$ THz/T, and its value is not a multiple of $\gamma_0$, so the resonance is not likely to be due to a multiple-magnon state. Second, this resonance appears in contradiction with the selection rule for the conventional ferrimagnetic resonance: The resonance should be absent when the oscillating magnetic field $\boldsymbol{H}^{\omega}$ is parallel to the spin direction. In our configuration, we set $\boldsymbol{H}^{\omega} \parallel \boldsymbol{H}$, meaning that some spin directions should be different from $\boldsymbol{H}$. However, this is expected at lower fields, while we see the resonance only in the high-field region. Moreover, we observed this resonance also in other polarized spectra, which hinders selection rules determination. In any case, we believe that it is some kind of ordered magnetic resonance.

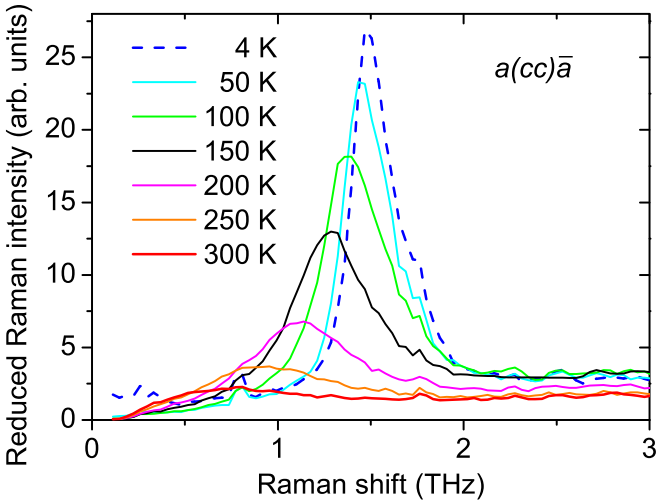


FIG. 5. Temperature dependence of $a(cc)\bar{a}$ Raman spectra showing the electromagnon. The high-frequency phonon spectra are in Fig. S2 in Ref. [25].

### D. Evolution of the electromagnon on $\boldsymbol{H} \parallel c$

We also measured THz spectra when applying $\boldsymbol{H} \parallel c$. Similarly to applying $\boldsymbol{H} \perp c$, we observed a suppression of the electromagnon intensity; this occurs at magnetic field values of ca. 2 T (see Fig. S4 in the Supplemental Material [25]). Furthermore, we also notice a hysteresis of the electromagnon intensity, closely related to that of the magnetization: Fig. 2(c) shows the magnetic-field dependence of the electromagnon strength [here defined as the integral of $k(\omega)$ over the frequency range of the peak] for $\boldsymbol{H} \parallel c$ at 150 K. The strength decreases the most at the transition from the ALC to the NLC magnetic structure, and the electromagnon is absent in the saturated state, where the spins are assumed to align collinearly along the $c$ direction.

As electromagnons are electric-dipole active, they contribute to the static dielectric permittivity. When an electromagnon is suppressed by the magnetic field, the static permittivity should decrease correspondingly. To verify this, we measured magnetic-field dependent low-frequency (1 kHz) dielectric permittivity $\varepsilon_c$ in the $c$ direction since the electromagnon is active for $\boldsymbol{E}^{\omega} \parallel c$. In Fig. 2(b), we see the expected decrease in the permittivity at the phase transition from the ALC to the NLC structure when the electromagnon is suppressed. To evaluate this sum rule quantitatively, we fitted the THz spectra by the Lorentz oscillator model. At zero field, the contribution of the electromagnon to the permittivity is 1.4. Assuming its contribution at 7 T to be zero (verified by

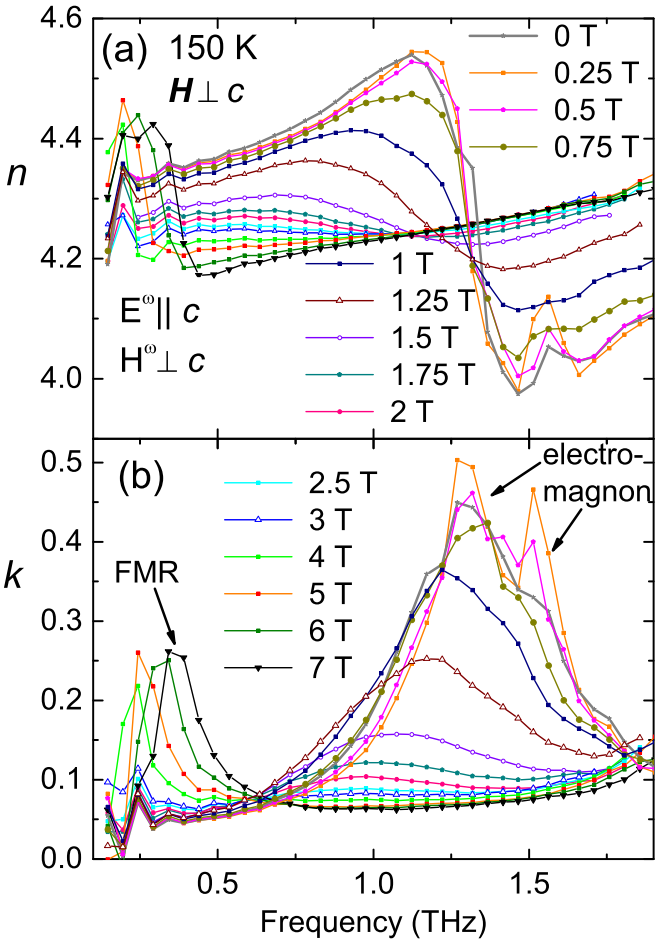


FIG. 6. THz spectra of (a) real and (b) imaginary part of refractive index as a function of external magnetic field $\boldsymbol{H} \perp c$ at 150 K with $\boldsymbol{E}^{\omega} \parallel c$, $\boldsymbol{H}^{\omega} \perp c$. All spectra were taken after applying high magnetic field and, therefore, the TC magnetic structure is assumed at low $\boldsymbol{H}$.

the fit), we expect the same step in the static permittivity; we observed a step of ≈1 [Fig. 2(b)] which is in a rough agreement. The mismatch may come from the conductivity contribution to the permittivity and/or from errors in the size and distance of electrodes of the measured capacitor.

Unfortunately, in Fig. 2 we could not compare the magnetic-field dependent permittivity with the electromagnon spectral weight at the same temperature, because the sample was leaky at 150 K and the electromagnon absorption was too high at 10 K (note that we were not able to determine the peak maximum in the $k$ spectrum, because the sample became opaque in this frequency range—see Fig. 4) For that reason the field dependencies of the permittivity and of the spectral weight are only qualitatively the same. The disappearance of electromagnons at higher magnetic field explains the decrease in permittivity at 1 kHz with increasing $H$—see Fig. 2.

### E. Microscopic origin of the electromagnon

We investigated the electromagnon activity in all principal directions of the dc magnetic field with respect to the crystallographic axes. We observed the electromagnon in the TC and ALC magnetic structures but not in the NLC and collinear ones (with spins in the $ab$ plane or along the $c$ axis). Such a comprehensive information enables us to apply to our observations the magnetostriction theory [10,20,21,27,28] describing electromagnons in related Y-type hexaferrites.

Since the $ab$ plane is magnetically isotropic, for describing magnetic states, we can employ a tetragonal basis instead of the hexagonal one; we assume axes $x$, $y$, $z$ in the new tetragonal basis coinciding with directions [1,0,0], [-1,2,0], [0,0,1] in the hexagonal system. Our task now is to employ the magnetostriction mechanism possibly inducing the electromagnon to all existing magnetic structures and to compare the analytically calculated selection rules with the experiment.

The polarization induced by spins according to the magnetostriction model reads

$$\vec{P} = \sum_{i,j} \vec{P}_{i,j} (\vec{S}_i \cdot \vec{S}_j), \tag{3}$$

where the summation involves the nearest neighbors within a magnetic unit cell, which can be quite large in modulated structures. Taking only nearest neighbors is relevant since spins are quite large in the block approximation (therefore they can be treated as classical), the next nearest neighbors are far apart from each other, and the superexchange interaction plays the most important role on boundaries of the blocks. The prefactor $\vec{P}_{i,j}$ must respect the crystal symmetry [22,38]. Taking the Y-hexaferrite crystal structure and the magnetic structure in the block approximation, the polarization along the $z$ axis has the following form [10,16,21]:

$$P_z \propto \sum_i \left( \vec{S}_i^{\,L} \cdot \vec{S}_i^{\,S} - \vec{S}_i^{\,S} \cdot \vec{S}_{i+1}^{\,L} \right). \tag{4}$$

For the dynamic ME effect, we assume all spins in Eq. (3) as time dependent, resulting in a time-dependent polarization $P_z(t)$. More specifically, we formally separate the static equilibrium spins known from the magnetic structure and the dynamical part. We assume the dynamical part to be small and perpendicular to the equilibrium spin direction, as the spin lengths must be conserved. As we are interested only in the dynamic ME effect, we omit the scalar products of static spins and take into account only the first-order dynamic terms of type $\vec{S}_1 \cdot \vec{\delta S}_2$, since the second-order terms of type $\vec{\delta S}_1 \cdot \vec{\delta S}_2$ are assumed to be small. Next, we separate the contributions to $P_z$ coming from $x$, $y$, and $z$ components of spins' deviations.

We now look for possible modes which can sum up constructively to the oscillating $P_z(t)$. The modes must not be magnetic-dipole active to be consistent with the experiment and, therefore, they should originate in spin vibration, not precession. The spin deviations are assumed to be proportional to the original spin lengths $S^L$, $S^S$. The static magnetic structures are described as follows: Among the TC structures, we take the one called 2-fan, described as [10,39]

$$\vec{S}_1^{\,S} = \begin{bmatrix} 0 \\ -S^S \cos(\theta^S) \\ S^S \sin(\theta^S) \end{bmatrix}, \quad \vec{S}_1^{\,L} = \begin{bmatrix} S^L \sin(\theta^L) \\ S^L \cos(\theta^L) \\ 0 \end{bmatrix},$$

$$\vec{S}_2^{\,S} = \begin{bmatrix} 0 \\ -S^S \cos(\theta^S) \\ -S^S \sin(\theta^S) \end{bmatrix}, \quad \vec{S}_2^{\,L} = \begin{bmatrix} -S^L \sin(\theta^L) \\ S^L \cos(\theta^L) \\ 0 \end{bmatrix},$$

where $\theta^L$ and $\theta^S$ denote the conical angles in the large and small blocks, respectively, taken from the $y$ axis [Fig. 1(g)].

For the LC structures, the situation is more complex, since there is also an incommensurate component, and the magnetic unit cell can be quite large. The length of the incommensurate modulation vector $\boldsymbol{Q}_{\mathrm{IC}}$ depends on temperature and it reaches a value of ca. 0.7 below 150 K [40]. For simplicity, we use the approximate value of 0.75 which is commensurate; then, the magnetic unit cell is only doubled compared to the TC structure and contains eight spins.

For the ALC structure, the spin configuration is as follows [10]:

$$\vec{S}_1^{\,S} = \begin{bmatrix} S^S \sin(\theta^S)\cos(\phi) \\ S^S \sin(\theta^S)\sin(\phi) \\ S^S \cos(\theta^S) \end{bmatrix}, \quad \vec{S}_1^{\,L} = \begin{bmatrix} 0 \\ -S^L \sin(\theta^L) \\ S^L \cos(\theta^L) \end{bmatrix},$$

$$\vec{S}_2^{\,S} = \begin{bmatrix} -S^S \sin(\theta^S)\cos(\phi) \\ S^S \sin(\theta^S)\sin(\phi) \\ -S^S \cos(\theta^S) \end{bmatrix}, \quad \vec{S}_2^{\,L} = \begin{bmatrix} S^L \sin(\theta^L) \\ 0 \\ -S^L \cos(\theta^L) \end{bmatrix},$$

$$\vec{S}_3^{\,S} = \begin{bmatrix} -S^S \sin(\theta^S)\cos(\phi) \\ -S^S \sin(\theta^S)\sin(\phi) \\ S^S \cos(\theta^S) \end{bmatrix}, \quad \vec{S}_3^{\,L} = \begin{bmatrix} 0 \\ S^L \sin(\theta^L) \\ S^L \cos(\theta^L) \end{bmatrix},$$

$$\vec{S}_4^{\,S} = \begin{bmatrix} S^S \sin(\theta^S)\cos(\phi) \\ -S^S \sin(\theta^S)\sin(\phi) \\ -S^S \cos(\theta^S) \end{bmatrix}, \quad \vec{S}_4^{\,L} = \begin{bmatrix} -S^L \sin(\theta^L) \\ 0 \\ -S^L \cos(\theta^L) \end{bmatrix},$$

and for the NLC structure:

$$\vec{S}_1^{\,S} = \begin{bmatrix} S^S \sin(\theta^S)\cos(\phi) \\ S^S \sin(\theta^S)\sin(\phi) \\ S^S \cos(\theta^S) \end{bmatrix}, \quad \vec{S}_1^{\,L} = \begin{bmatrix} 0 \\ -S^L \sin(\theta^L) \\ -S^L \cos(\theta^L) \end{bmatrix},$$

$$\vec{S}_2^{\,S} = \begin{bmatrix} -S^S \sin(\theta^S)\cos(\phi) \\ S^S \sin(\theta^S)\sin(\phi) \\ S^S \cos(\theta^S) \end{bmatrix}, \quad \vec{S}_2^{\,L} = \begin{bmatrix} S^L \sin(\theta^L) \\ 0 \\ -S^L \cos(\theta^L) \end{bmatrix},$$

$$\vec{S}_3^{\,S} = \begin{bmatrix} -S^S \sin(\theta^S)\cos(\phi) \\ -S^S \sin(\theta^S)\sin(\phi) \\ S^S \cos(\theta^S) \end{bmatrix}, \quad \vec{S}_3^{\,L} = \begin{bmatrix} 0 \\ S^L \sin(\theta^L) \\ -S^L \cos(\theta^L) \end{bmatrix},$$

$$\vec{S}_4^{\,S} = \begin{bmatrix} S^S \sin(\theta^S)\cos(\phi) \\ -S^S \sin(\theta^S)\sin(\phi) \\ S^S \cos(\theta^S) \end{bmatrix}, \quad \vec{S}_4^{\,L} = \begin{bmatrix} -S^L \sin(\theta^L) \\ 0 \\ -S^L \cos(\theta^L) \end{bmatrix}.$$

In both cases, the helical angle $\phi = 45^\circ$ for $\boldsymbol{Q}_{\mathrm{IC}} = (0,0,0.75)$, and the relative phase of small and large spin modulations is 180°.

The criterion for $P_z(t)$ via the magnetostriction is the appearance of oscillating ↑-↑-↓-↓ spin structure where spins can point in any direction. Taking, for example, the 2-fan structure and spin components in the $z$ direction, the static magnetic structure is ↑-0-↓-0, leading to zero static $P_z$. However, if we add small spin deviations with ↑-↑-↓-↓ amplitudes, we can get oscillating $P_z$—this is exactly the so-called out-of-phase mode, proposed by Nakajima *et al.* [21]. As the spins oscillate in the $z$ direction, we then call it $z$ mode. In the $xy$ plane, we can find another mode contributing constructively to $P_z(t)$, where the neighboring small spins oscillate in opposite directions along $x$ axis and the large spins are not involved; we call this the $x$ mode. On the other hand, all oscillations in the $y$ direction (the cone axis) add up destructively, yielding no contribution to $P_z(t)$. Altogether, in the 2-fan structure, we can expect 2 modes which are listed in Table I.

The two LC structures differ just in $z$-spin components. The ALC structure has either a ↑-↑-↓-↓ $z$-component spin structure yielding even static $P_z$ or a ↑-0-↓-0 structure with $P_z = 0$. Nevertheless, in both cases, adding ↑-↑-↓-↓ spin deviations in the $z$ direction can lead to oscillating $P_z$ as in the case of the 2-fan structure via the $z$ mode. In contrast, in the NLC structure, $z$-spin components add up always destructively yielding no oscillating $P_z$, as demonstrated in Table I.

For the two LC structures in the $xy$ plane, the oscillations in the $x$ and $y$ directions are equivalent with the same frequency and have to be represented as one mode because of the constraint that the spins deviations must be perpendicular to the original spin direction. This mode summing constructively was proposed by Nakajima *et al.* [10]; it corresponds to clockwise deviations of small spins and counterclockwise deviations of large spins in the $xy$ plane, and we call it here the $xy$ mode.

Altogether, there are two distinct modes contributing to the $P_z(t)$ in 2-fan and ALC structures, and one mode in the NLC structure, as summarized in Table I.

From the comparison of our analytical calculations and observations, it appears that the strong absorption in the THz spectra is due to spin oscillations in the $z$ direction. In fact, we observe the electromagnon in the 2-fan and ALC phases but not in the NLC one, and the decrease in its strength is the most pronounced at the phase transition from the ALC to the NLC phase. In principle, the strong absorption in the ALC structure could be due to the $xy$ mode, which was proposed by Nakajima *et al.* [21] for the related Y-hexaferrite $BaSrCo_2Fe_{11}AlO_{22}$ and confirmed by inelastic neutron scattering. Then, the decrease in the electromagnon strength at the ALC–NLC phase transition would be caused by the spins inclining towards the $z$ axis as we apply the magnetic field along $z$, because the spin system would approach the collinear phase. Nevertheless, the abrupt change in the electromagnon strength supports the $z$ mode as an origin of the strong electromagnon absorption, because no such change in magnetization was observed at the corresponding fields [cf. Figs. 2(a) and 2(c)].

As the spin deviations are perpendicular to the original spin directions, there are additional constraints (last column in Table I), providing an insight into the dependence of the oscillating polarization on conical angles entering into the formulas for the polarization (second column in Table I). First, any deviation is proportional to the original spin direction, so all terms contain the prefactor $S^L S^S$. Only in the case of $z$ mode in the ALC structure do additional constraints yield nontrivial dependencies of the oscillating polarization on the conical angle: $P_z(t) \propto \cos(\theta^L)\sin(\theta^S) + \cos(\theta^S)\sin(\theta^L)$, which, for $\theta^L = \theta^S = \theta$, becomes $P_z \propto \sin(2\theta)$, providing the maximum

value of electromagnon absorption at an angle of 45°. Such a nontrivial dependence can be the reason why the electromagnon strength first increases with magnetic field and starts decreasing only at ≈1 T [Fig. 2(c)]. However, this dependence may be also caused by a more disordered, probably mixed magnetic structure, leading to a stronger absorption at ≈1 T. Finally, the selection rules for the ALC phase could explain the double-peak structure in ZFC spectra (Fig. 4)—the $xy$ and $z$ modes may appear simultaneously and contribute at different frequencies.

For the 2-fan structure, the predicted dependence of the electromagnon strength on the conical angle is monotonic, $P_z \propto \sin(\theta)$. In the experiment, we see some deviations from this behavior. Surprisingly, at first, the intensity of the electromagnon increases with magnetic field, reaching a maximum at 0.25 T; only then it starts to decrease (Fig. 6). Notice that when reaching $\mu_0 \boldsymbol{H} \approx 0.25$ T, a single-domain 2-fan structure is established. It is worth noting that in $BaSrCo_2Fe_{11}AlO_{22}$, at similar fields, Nakajima *et al.* observed a similar behavior—a maximum in the neutron diffraction intensity [10] which was not completely explained either. Our observation can have three explanations: First, the zero-field magnetic structure was not single-phase TC. Second, the single domain state provides a constructive interference of polarization in the material and that of the electromagnetic wave. Third, going beyond the block approximation and assuming spin directions varying within the blocks, the magnetostriction term may depend differently on the spin configuration, similarly to the case of the ALC structure. This would cause the highest absorption to occur at a general angle between 0° and 90°, as proposed by Kida *et al.* [27].

Let us now comment on the double-peak structure seen in the range from 0 T to 0.75 T and observed the most clearly at 0.25 T [Fig. 6(b)]. This feature is not seen in the ZFC spectra plotted in Fig. 4; it may be due to different magnetic-field histories and it may be connected with the 2-fan state but not with the ALC one. In the 2-fan structure, two electromagnon modes are allowed, which may explain the observed two peaks.

Last but not least, we note that in Table I we listed just purely electrically active (i.e., vibrational) modes caused by magnetostriction. We neglected the influence of ac magnetic field on these modes, and we did not analyze other possible magnetic-field-active modes (one of them describing possibly the low-frequency resonance seen in Fig. 6 below 0.4 THz). To this aim, we would need to treat the spin Hamiltonian appropriate for this compound which is still an unresolved question, as so-far-proposed Hamiltonians were not able to describe all magnetic structures observed in Y-hexaferrites.

Finally, it is obvious that not all minor features in spectra can be explained by the simple theory. To this aim, one would have to dispose of a detailed knowledge of the spin configuration which would make it possible to go beyond the block approximation.

## IV. CONCLUSION

In conclusion, we investigated experimentally static and dynamic magnetoelectric properties of the Y-type hexaferrite $BaSrCoZnFe_{11}AlO_{22}$. Its magnetic structures were determined by static magnetization measurements, and a purely electric-dipole active electromagnon was observed by THz and Raman spectroscopies. The Raman intensity of the electromagnon was unusually high. We suggest that this is due to an anomalously high susceptibility of frustrated magnetic structure, but this hypothesis would require deeper theoretical clarification. We also studied in detail the properties of the electromagnon in various magnetic phases determined by the magnetic-field direction and history. Using a magnetostriction model, it was possible to identify the origin of the electromagnon to explain its magnetic-field dependence and to correlate the electromagnon strength with the static magnetodielectric properties. We described the dominant features in the field dependence of the spectra, but some minor ones remain unexplained. In order to gain an even deeper insight into the observed behavior, more sophisticated theories, going beyond the block approximations, would be probably required.

## ACKNOWLEDGMENTS

The authors thank Jan Prokleška, Vladimír Tkáč, Petr Proschek, Jan Drahokoupil, Karel Jurek, and Štěpán Huber for their help with experiments and Titusz Fehér for helpful discussions. This work was supported by the Czech Science Foundation (Projects No. 15-08389S and No. 18-09265S), the program of the Czech Research Infrastructures, Project No. LM2011025 and the MŠMT Project No. LD15014. J. Vít was partially supported by the Grant Agency of the Czech Technical University in Prague, Grant No. SGS16/244/OHK4/3T/14. Y. S. Chai, K. Zhai, and Y. Sun are supported by the National Natural Science Foundation of China (Grants No. 11534015, No. 11674384, and No. 11675255).

[1] Y. Kitagawa, Y. Hiraoka, T. Honda, T. Ishikura, H. Nakamura, and T. Kimura, Nat. Mater. **9**, 797 (2010).
[2] T. Kimura, Annu. Rev. Condens. Matter Phys. **3**, 93 (2012).
[3] Y. S. Chai, S. Kwon, S. H. Chun, I. Kim, B.-G. Jeon, K. H. Kim, and S. Lee, Nat. Commun. **5**, 4208 (2014).
[4] K. Zhai, Y. Wu, S. Shen, W. Tian, H. Cao, Y. Chai, B. C. Chakoumakos, D. Shang, L. Yan, F. Wang *et al.*, Nat. Commun. **8**, 519 (2017).
[5] S. Ishiwata, Y. Taguchi, H. Murakawa, Y. Onose, and Y. Tokura, Science **319**, 1643 (2008).
[6] F. Wang, T. Zou, L.-Q. Yan, Y. Liu, and Y. Sun, Appl. Phys. Lett. **100**, 122901 (2012).
[7] R. C. Pullar, Prog. Mat. Sci. **57**, 1191 (2012).
[8] N. Momozawa, Y. Yamaguchi, H. Takei, and M. Mita, J. Phys. Soc. Jpn. **54**, 771 (1985).
[9] M. Soda, T. Ishikura, H. Nakamura, Y. Wakabayashi, and T. Kimura, Phys. Rev. Lett. **106**, 087201 (2011).
[10] T. Nakajima, Y. Tokunaga, M. Matsuda, S. Dissanayake, J. Fernandez-Baca, K. Kakurai, Y. Taguchi, Y. Tokura, and T.-h. Arima, Phys. Rev. B **94**, 195154 (2016).

[11] H. B. Lee, Y.-S. Song, J.-H. Chung, S. H. Chun, Y. S. Chai, K. H. Kim, M. Reehuis, K. Prokeš, and S. Mat'aš, Phys. Rev. B **83**, 144425 (2011).
[12] I. A. Sergienko and E. Dagotto, Phys. Rev. B **73**, 094434 (2006).
[13] H. Katsura, A. V. Balatsky, and N. Nagaosa, Phys. Rev. Lett. **98**, 027203 (2007).
[14] T. Kimura, G. Lawes, and A. P. Ramirez, Phys. Rev. Lett. **94**, 137201 (2005).
[15] S. Hirose, K. Haruki, A. Ando, and T. Kimura, Appl. Phys. Lett. **104**, 022907 (2014).
[16] S.-P. Shen, X.-Z. Liu, Y.-S. Chai, A. Studer, K. Rule, K. Zhai, L.-Q. Yan, D.-S. Shang, F. Klose, Y.-T. Liu *et al.*, Phys. Rev. B **95**, 094405 (2017).
[17] S. Shen, Y. Chai, and Y. Sun, Scient. Rep. **5**, 8254 (2015).
[18] Y. S. Chai, S. H. Chun, J. Cong, and K. H. Kim, arXiv:1712.05928.
[19] M. Matsumoto, K. Chimata, and M. Koga, J. Phys. Soc. Jpn. **86**, 034704 (2017).
[20] N. Kida, D. Okuyama, S. Ishiwata, Y. Taguchi, R. Shimano, K. Iwasa, T. Arima, and Y. Tokura, Phys. Rev. B **80**, 220406(R) (2009).
[21] T. Nakajima, Y. Takahashi, S. Kibayashi, M. Matsuda, K. Kakurai, S. Ishiwata, Y. Taguchi, Y. Tokura, and T.-h. Arima, Phys. Rev. B **93**, 035119 (2016).
[22] P. Wang, X. Lu, X. Gong, and H. Xiang, Computat. Mater. Sci. **112**, 448 (2016).
[23] N. Momozawa, M. Mita, and H. Takei, J. Cryst. Growth **83**, 403 (1987).
[24] P. Kužel and J. Petzelt, Ferroelectrics **239**, 79 (2000).
[25] See Supplemental Material at http://link.aps.org/supplemental/10.1103/PhysRevB.97.134406 for additional magnetization measurements, THz, infrared and Raman spectra, more detailed discussion of infrared and Raman activity of the phonons and the electromagnon, and determination of errors in time-domain THz transmission spectroscopy.
[26] S. Shen, L. Yan, Y. Chai, J. Cong, and Y. Sun, Appl. Phys. Lett. **104**, 032905 (2014).
[27] N. Kida, S. Kumakura, S. Ishiwata, Y. Taguchi, and Y. Tokura, Phys. Rev. B **83**, 064422 (2011).
[28] N. Kida, Y. Takahashi, J. Lee, R. Shimano, Y. Yamasaki, Y. Kaneko, S. Miyahara, N. Furukawa, T. Arima, and Y. Tokura, J. Opt. Soc. Am. B **26**, A35 (2009).
[29] In principle, we could have made the sample thinner and resolve the spectra with high absorption. However, we possess just one exemplar of the crystal and plan other measurements with it, so we decided to keep the crystal as a whole.
[30] S. Kamba, V. Goian, M. Savinov, E. Buixaderas, D. Nuzhnyy, M. Maryško, M. Kempa, V. Bovtun, J. Hlinka, K. Knížek *et al.*, J. Appl. Phys. **107**, 104109 (2010).
[31] S. Skiadopoulou, V. Goian, C. Kadlec, F. Kadlec, X. F. Bai, I. C. Infante, B. Dkhil, C. Adamo, D. G. Schlom, and S. Kamba, Phys. Rev. B **91**, 174108 (2015).
[32] J. Buhot, C. Toulouse, Y. Gallais, A. Sacuto, R. De Sousa, D. Wang, L. Bellaiche, M. Bibes, A. Barthélémy, A. Forget *et al.*, Phys. Rev. Lett. **115**, 267204 (2015).
[33] U. Nagel, R. S. Fishman, T. Katuwal, H. Engelkamp, D. Talbayev, H. T. Yi, S.-W. Cheong, and T. Rõõm, Phys. Rev. Lett. **110**, 257201 (2013).
[34] J. H. Lee, I. Kézsmárki, and R. S. Fishman, New J. Phys. **18**, 043025 (2016).
[35] P. Fleury and R. Loudon, Phys. Rev. **166**, 514 (1968).
[36] S. Kamba, F. Borodavka, F. Kadlec, C. Kadlec, Y. S. Chai, K. Zhai, Y. Sun, and J. Vít, Ferroelectrics (to be published).
[37] F. Kadlec, C. Kadlec, J. Vít, F. Borodavka, M. Kempa, J. Prokleška, J. Buršík, R. Uhrecký, S. Rols, Y. S. Chai *et al.*, Phys. Rev. B **94**, 024419 (2016).
[38] I. A. Sergienko, C. Şen, and E. Dagotto, Phys. Rev. Lett. **97**, 227204 (2006).
[39] A. J. Hearmon, R. D. Johnson, T. A. W. Beale, S. S. Dhesi, X. Luo, S.-W. Cheong, P. Steadman, and P. G. Radaelli, Phys. Rev. B **88**, 174413 (2013).
[40] H. Ueda, Y. Tanaka, Y. Wakabayashi, and T. Kimura, Physica B (2017), doi:10.1016/j.physb.2017.09.061.